



HAL
open science

S=1/2 chain in BiVO₃F: spin-dimers versus photoanodic properties

Olivier Mentré, Miguel A Juárez-Rosete, Sebastien Saitzek, Cintli Aguilar-Maldonado, Marie Colmont, Ángel M Arévalo-López

► **To cite this version:**

Olivier Mentré, Miguel A Juárez-Rosete, Sebastien Saitzek, Cintli Aguilar-Maldonado, Marie Colmont, et al.. S=1/2 chain in BiVO₃F: spin-dimers versus photoanodic properties. *Journal of the American Chemical Society*, 2021, 143 (18), pp.6942-6951. 10.1021/jacs.1c00621 . hal-03290791

HAL Id: hal-03290791

<https://hal.science/hal-03290791>

Submitted on 19 Jul 2021

HAL is a multi-disciplinary open access archive for the deposit and dissemination of scientific research documents, whether they are published or not. The documents may come from teaching and research institutions in France or abroad, or from public or private research centers.

L'archive ouverte pluridisciplinaire **HAL**, est destinée au dépôt et à la diffusion de documents scientifiques de niveau recherche, publiés ou non, émanant des établissements d'enseignement et de recherche français ou étrangers, des laboratoires publics ou privés.

S=1/2 chain in BiVO₃F: spin-dimers versus photoanodic properties

Olivier Mentré*, Miguel A. Juárez-Rosete, Sebastien Saitzek, Cintli Aguilar-Maldonado, Marie Colmont, Ángel M. Arévalo-López

Univ. Lille, CNRS, Centrale Lille, Univ. Artois, UMR 8181, UCCS, Unité de Catalyse et Chimie du Solide, F-59000 Lille, France

*: Corresponding author, email : Olivier.mentre@univ-lille.fr

Abstract: BiVO₃F was prepared, characterized and identified as the unique example of bismuth vanadyl oxyhalide with paramagnetic V⁴⁺ centres. Its crystal structure shows 1D magnetic units with rare alternation of edge sharing O-O and F-F μ_2 bridges along the octahedral chains. Structural pairing across the O₂ edges induces antiferromagnetic spin dimers(S=0) with $J/K_b \sim 300K$, ~ 15 times greater than the exchange across the F₂ bridges, within a non-ordered magnetic ground state. Despite multiple compositional, structural, and electronic analogies with the BiVO₄ scheelite compound, one of the most promising photo-anode for solar water splitting, the photo activity of BiVO₃F is relatively modest, partially due to this electronic pairing playing for fast electron-hole recombination. Similar to monoclinic-VO₂, the V⁴⁺ spin dimerization plays against the singlet \rightarrow triplet electronic photo-excitation, but brings potential carrier lifetime benefits. The reduction of the bandgap from $E_g \sim 2.4$ eV to ~ 1.7 eV after incorporation of d^1 cations in BiVO₄ makes BiVO₃F an inspiring compound for local modifications toward an enhanced photo-active material. The direct $d \rightarrow d$ transition provides a significant enhancement of the visible light capture section, and opens a prospective route for the chemical design of performant photoanodes with a mixed anionic sublattice.

Introduction: Inorganic metal oxide-fluorides have significant importance in recent technologies, such as, energy storage¹, microelectronics^{2,3,4}, photonics and catalysis.⁵ Within this frame, the recent discovery of the $n=1$ Aurivillius oxyfluoride $[\text{Bi}_2\text{O}_2][\text{CoF}_4]$ phase has opened even wider perspectives about novel multiferroics⁶ by combining ferroelectric opportunities brought by standard Bi^{3+} lone-pair effect, and magnetic ordering brought from the presence of magnetic ions in the $[\text{CoF}_4]$ perovskite block, mimicking BiFeO_3 . Besides, due to the similarity on their ionic radii, the replacement of O^{2-} by F^- in flexible structural motifs such as perovskite or rocksalt blocks allows the O^{2-}/F^- random distribution and may accommodate anionic vacancies (v) and subtle metal displacements, as in $\text{AM}(\text{O},\text{F},v)_3$, BaInO_2F or $\text{FeO}_{1-x}\text{F}_x$ ⁷. However, the 1D (chain-based) oxy-fluorides topology⁸ often induces anionic ordering, especially when surrounded by lone-pair ions with anisotropic electronic density clouds. Such oxyfluoride chains have provided excellent models for low dimensional magnetism, due to the minimization of electronic delocalization through electronegative F^- bridges⁹. Up to date, the concerned $\text{Bi}-\text{V}-\text{O}-\text{F}$ chemical system is almost empty, since only 3D F^- doped- BiVO_4 ¹⁰ and $\text{Bi}_2\text{VO}_5\text{F}$ ¹¹ have been reported so far. In the former, the F^- doping enables enhanced photoelectrochemical performances, while the later corresponds to F^- doping in the perovskite slabs of the well know 2D- $\text{Bi}_4\text{V}_2\text{O}_{11}$, the best high temperature ionic conductor ever, and thus, induces a minor amount of V^{4+} .

We report in here the synthesis of the first bismuth vanadyl oxyhalide BiVO_3F . It shows a unique alternation of O_2 and F_2 bridges in $\text{V}^{4+}(S=1/2)$ chains which offer nice perspectives for the design of materials straddling the border between finite clusters and periodic magnetic lattices. In addition, the compositional analogy between BiVO_3F and BiVO_4 , one of the most promising photoanode for water splitting¹², suggests photoelectronic activities. In the latter oxide, the conduction band (CB) containing $3d^0 \text{V}^{5+}$ hybridized with $\text{O}2p$ states form large polarons beneficial as catalytic redox centers for screening the carrier-carrier and carrier-defect scattering in favor of long carrier lifetime¹³ together with raising of the valence band (VB) edge and bandgap reduction from the low binding energy states of $\text{Bi}^{3+} 6s^2$ electrons. Strategies for enhanced BiVO_4 photocatalytic properties have been proposed by tuning its electronic structure with chemical substitution using either less electronegative anions (S^{2-} , N^{3-}) or cations with occupied low binding energy d^{10} states (Cu^+ , Ag^+) with inherent chemical problems¹³. Theoretical incorporation of unfilled d^n cations ($d^1 \text{Cr}^{5+}$, Mo^{5+} , W^{5+}) has shown favorable separation of photo-excited electron-hole pairs, giving opportunities of the electrons to transit from VB to CB for the reduction of the electron effective mass and lengthening of the carrier diffusion.¹⁴ Similar to the Fe^{3+} doped TiO_2 situation, where the dopant $d-d$ transitions offer visible light response due to narrowing of the band gap, trapping of electron and hole and decrease of excitons recombination.¹⁵ Closer to the title compound, V^{4+} self-doped $\text{BiVO}_{4-\delta}$ nanorods prepared in solvothermal conditions also show enhanced organic pollutant degradation under visible light assigned to the improved electron-hole separation.¹⁶ Similar photocatalytic performances have been reported for microporous F^- -doped BiVO_4 obtained after autoclave reaction with NH_4F ¹⁷ however, no reliable crystallographic evidences of the intrinsic vanadium reduction has been given, along with a weak bandgap evolution, thus suggesting synergical surficial and microstructural effects.

The introduction of $d^1 \text{V}^{4+}$ species with direct $d-d$ excitations and narrowed bandgap in BiVO_3F makes this phase a model to investigate its characteristic electronic structure features. It also opens a new route and inspiring concepts to tune photo-anodic properties by mixed anion content control.¹⁸

Results and Discussion

1D crystal Structure: Single crystals of BiVO_3F have been grown through hydrothermal route from a 2:1 mixture of VF_3 (or VF_4) and Bi_2O_3 in a dilute HF solution. BiVO_3F can be obtained as the main phase when working out of stoichiometry in a $\text{Bi}:\text{V} = 1:2$ ratio, while when working in stoichiometric conditions results on the major co-presence of BiOF and $\text{Bi}_7\text{F}_{11}\text{O}_5$ bismuth oxyfluorides. Using the former procedure either single crystals can be selected, or a $\sim 90\text{w}\%$ polycrystalline can be achieved after several sonication in ethanol/separations stages from the later (see details in Supplementary materials, S1). Contrarily to the reported F^- doped BiVO_4 samples¹⁷, announced with a scheelite lattice independent of the Bi/F ratio, our results evidence drastic changes driven by V^{4+} and F^- incorporation in the lattice. It is plausible that the final firing stage in air at 450°C favors surficial and microstructural V^{4+} and F^- defects only. The BiVO_3F crystal structure was solved from single crystal X-ray diffraction (XR) data ($R_{\text{obs}} = 1.81\%$, $wR_{\text{obs}} = 2.05\%$) in the monoclinic $P2_1/n$ space group ($a = 5.2621(6) \text{ \AA}$, $b = 4.9721(3) \text{ \AA}$, $c = 12.6149(7) \text{ \AA}$, $\beta = 95.590(2)^\circ$, $V = 328.48(3) \text{ \AA}^3$, $Z = 4$), See Supplementary Table S2 for details. The pertinent bond distances are given in Table 1 (CSD 2055766). The crystal structure consists of edge-sharing $\infty[\text{V}^{4+}\text{O}_3\text{F}]^{3-}$ zigzag chains separated by Bi^{3+} cations, see Fig.1a and b. The asymmetric Bi^{3+} coordination is typical of $6s^2$ lone-pair (E) ions with a $3\text{O} + \text{E}$ basal plane and shifted $2\text{O} + 2\text{F}$ axial ligands. The anions are clearly distinguished by their Bond Valence Sums (BVS) with values in between -1.82 and -2.26 for $\text{O}1-3$ and -0.97 for F , see S3-S5.

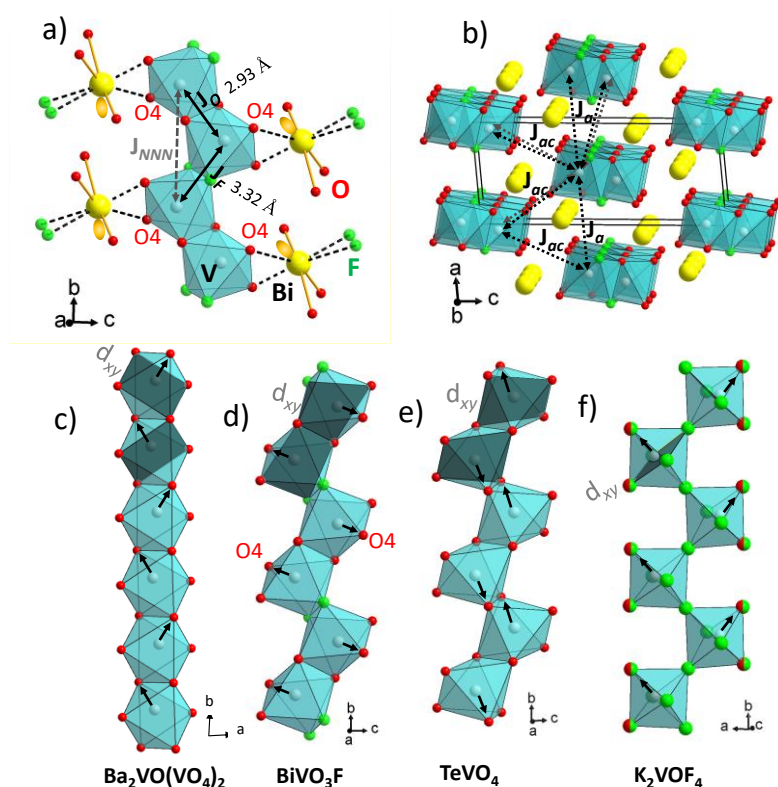


Figure 1. a) $\infty[\text{V}^{4+}\text{O}_3\text{F}]^{3-}$ zigzag chains of edge-shared VO_4F_2 octahedra and interstitial Bi^{3+} with intra-chains $\text{V}-\text{V}$ couplings. b) Main inter-chain exchanges considered. Comparison of vanadyl-chain topology and d_{xy} magnetic orbitals (darkened planes) in c) $\text{Ba}_2\text{VO}(\text{VO}_4)_2$, d) BiVO_3F , e) TeVO_4 and c) K_2VOF_4 . The arrows picture the $\text{V}=\text{O}$ short bonds.

Table 1. Interatomic distances (\AA) and cation BVS for BiVO_3F structure.

Bond	Dist. (\AA)	Bond	Distance (\AA)
Bi—O1	2.102(7)	V—O1	1.938(8)
Bi—O2	2.165(8)	V—O1	1.919(8)
Bi—O2	2.135(8)	V—O2	1.996(8)
Bi—O3	2.833(8)	V—O3	1.641(9)
Bi—O3	2.642(9)	V—F	1.991(7)
Bi—F	2.831(7)	V—F	2.154(7)
Bi—F	2.776(6)	$\Sigma_i S_i$	4.09(5)
$\Sigma_i S_i$	4.09(5)	V—V _(O2)	2.935(3)
		V—V _(F2)	3.320(3)

The zig-zag chains of BiVO_3F are similar to those found in pyroxene, but rely on the *cis* – *trans* alternation of O-O and F-F μ_2 bridges along the *b*-axis. To the best of our knowledge, such sequential O-O and F-F bridges, along edge-sharing chains have only been reported for $\text{Na}_2\text{Fe}(\text{PO}_4)\text{F}$ ¹⁹, $\text{Fe}(\text{SeO}_3)\text{F}$ ²⁰ and $\text{M}_2(\text{XO}_3)\text{F}_2$ ($\text{M}=\text{Mn, Co, Ni, Cu}$; $\text{X}=\text{Te, Se}$)^{21, 22} where the oxygen ions are systematically corners of covalent oxo-anion groups in contrast with BiVO_3F . Despite its 1D- crystal structure, a certain analogy with the 0D- BiVO_4 exists due to the conservation of trigonal planar coordination for O1, O2 and O3 and the strongly acentric coordination of Bi^{3+} ions. The hypothetical topochemical $\text{BiVO}_4 \rightarrow \text{BiVO}_3\text{F}$ transformation can be sketched in three main steps, see Fig.2. i) starting from the scheelite BiVO_4 , the VO_4 groups are tilt and displaced towards each other by pairs. ii) this leaves large voids for F^- insertion, i.e. 1F^- per VO_4 , while VO_4 approach tend to a common O-O edge. At this stage Bi^{3+} species would be displaced by *push and pull* mechanism in the (*bc*) plane. iii) The BiVO_3F crystal structure will then merge O-O and F-F edges into 1D chains. This synopsis inspires the possibility of an experimental scenario by controlled fluorination.

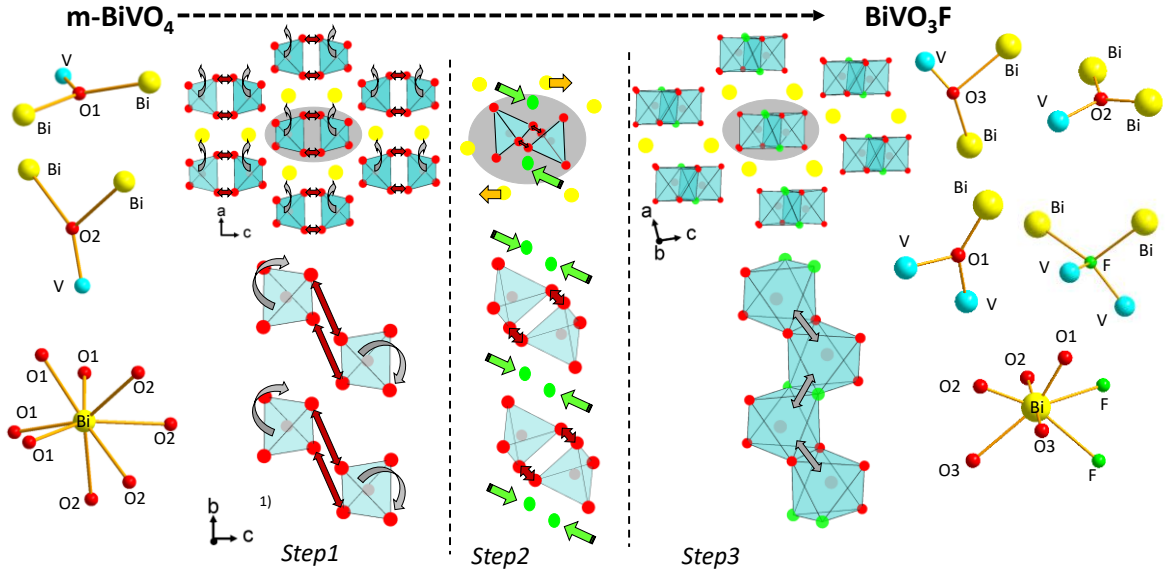


Figure 2: Detail of the anion and Bi coordination and sketch of a hypothetical structural transformation of monoclinic- BiVO_4 into BiVO_3F in 3 steps according to the main text.

BiVO_3F offers a unique opportunity to examine the magnetic M-O-M versus M-F-M superexchange in a single material, without of the engagement of oxygen ions in counter polyanions on the oxygen mediating corner, such as PO_4 , SeO_3 and TeO_3 in the compounds mentioned above.¹⁹⁻²² Here the octahedral distortion due to the V=O vanadyl bond externally to the chain-

axis and the O/F ordering shifts the super-exchange angle from $\sim 90^\circ$ as observed in some pyroxenes with similar canted chains²³ to V-O-V/V-F-V = 99.0(3) ° /106.4(3) ° close to what found in α -TeVO₄.^{24, 25} Despite the vanadyl bonds, a significant V⁴⁺-V⁴⁺ pairing occurs along the chains, with distances of 2.93 Å and 3.32 Å across O-O and F-F bridges respectively, despite short vanadyl bonds occurring externally to the V-V axis. The coulombic repulsion associated with the (V = O)²⁺ ions induces a crystal field splitting of the t_{2g} levels, such that the magnetic d¹ electrons lie mainly on the d_{xy} orbital accordingly to the darkened planes in Fig.1c-f. Here, the zig-zag edge-sharing chain topology and vanadyl arrangement of BiVO₃F (Fig.1d) are compared to i) linear chains in Ba₂(VO)(VO₄)₂²⁵ with weakened intra-chain exchanges (V-O-V = 96°) but reinforced inter-chain couplings, Fig.1c. ii) α -TeVO₄ a rare example of double-vanadyle bonds towards a common edge with frustration between ferromagnetic (FM) Nearest Neighbors (NN) and antiferromagnetic (AFM) Next Nearest Neighbors (NNN) exchanges along the chain-axis, Fig.1e. iii) the anion disordered K₂VOF₄ in which successive magnetic orbitals are perpendicular, along the chain, returning to paramagnetic behavior down to 2 K²⁶, Fig.1f.

V⁴⁺ spin dimers: In BiVO₃F, the overlap between magnetic orbitals across the electronegative F-F bridge appears poorly efficient, with detrimental M-F long bond scaling effects²⁷ see Fig.1d. In contrast, the d_{xy} orbital are coplanar across the O-O μ_2 bridge leaving an ideal topology for σ bonds. However, the V-V direct exchanges are expected weak because V-V is slightly above the reported V⁴⁺ critical distance 2.9 Å²⁸. The influence of the anion crystal field strength was first determined by Extended Hückel Tight-Binding calculations (EHBT), changing the O²⁻, F⁻ concentration. Thus, we have conserved the experimental geometry of isolated V₂O₆F₄ units and compared it with the extremes V₂F₁₀ and V₂O₁₀ units, a drastic effect is observed on the crystal field splitting D_q and Racah B, C parameters. The standard quadratic split of (V = O)²⁺ ions is exaggerated due to mixed O²⁻/F⁻ coordination and to the structural pairing across the O₂ edge, but its fingerprint prevails in the spectroscopic terms: ²T₂ → ²B₂ and ²E ; ²E_g → ²B₁ and ²A₁ highlighted in Fig. 3a for the experimental dimer.²⁹ The effect of the ligand field well reproduces the T₂/E_g increasing split from the *weak* fluoride crystal field D_q/B to the *medium* oxygen crystal field, similar to that reported for CrF₆ /CrO₆ octahedral units.³⁰ In addition, the well-known tendency of electronegative F⁻ anions to lower the valence band (VB) states was also evidenced, schematized by yellow arrows in Fig. 3a. Focusing on the V₂O₆F₄ real unit shown on Fig. 3b, the molecular orbital levels calculated by EHBT are shown in Fig. 3c, d. For a dimer cluster, the commonly calculated energy splittings observed for most of the levels is due to the intermolecular orbital interaction based on the Hückel approximation. For increasing chain lengths, the bandwidth would approaches the value of an infinite chain.³¹ The highest occupied molecular orbitals (HOMO) correspond to a magnetic S = 0 paired singlet, through degenerate $\sigma^* V_{dxy}-(O_{py})-V_{dxy}$ and $\sigma V_{dxy}-(O_{px})-V_{dxy}$ overlaps.

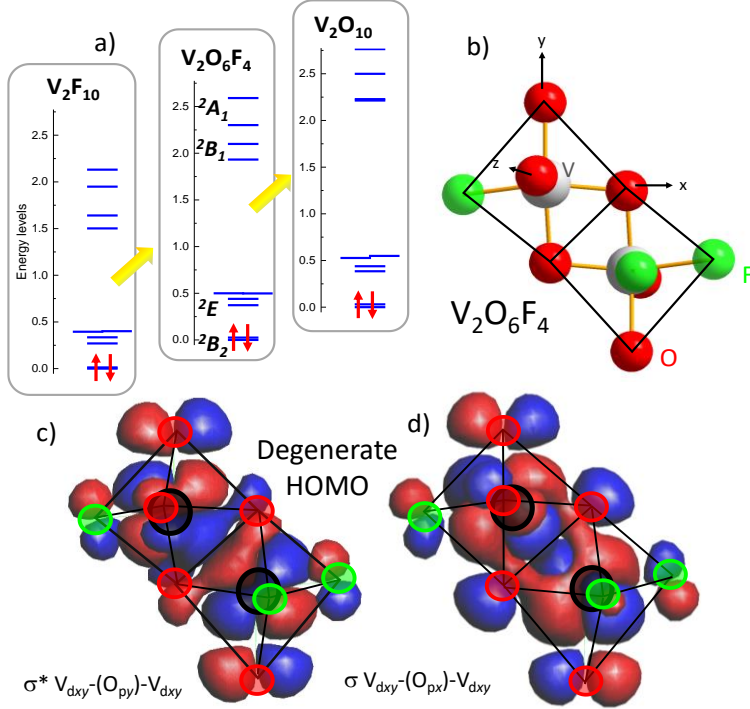


Figure 3. a) EHTB molecular orbital energy levels calculated for isolated V_2F_{10} , $V_2O_6F_4$ and V_2O_{10} units, b) structural view of the $V_2O_6F_4$ selected dimer. c) $\sigma^* V_{dxy}-(O_{py})-V_{dxy}$ and d) $\sigma V_{dxy}-(O_{px})-V_{dxy}$ degenerate HOMO's corresponding to the 2B_2 levels of Fig.3c.

Magnetic Topology: The main identified magnetic exchanges for $BiVO_3F$ are shown Fig. 1, named J_O and J_F intra-chain and J_{ac} and J_a inter-chain exchanges with respect to V-V distances lower than 6\AA . Keeping in mind the particularly ambiguous choice of the Hubbard term U for V^{4+} , made on empirical grounds³², we mapped the total energies for a number of collinear spin configurations into a classical Heisenberg model to yield individual exchange couplings for different $U = 2 - 4$ eV and the effective on-site exchange interaction $J_{\text{eff}} = 1$ eV. Results are listed Table 2 together with the calculated bandgap and can be crosschecked to the experimental values from our $\chi(T)$ fit and uv-visible reflectance spectroscopy. The super-exchange (SE) J_O across the O-O bridge is predominant and larger than J_F by more than one order of magnitude for all U values, while exchange J_{NNN} is very weak and almost U -independent. This results in a strong dimeric system already at room temperature, in accordance with the blank EPR signal measured from room temperature down to 4 K (X-Band, Brüker ELEXYS E580) where the $S=1$ state is poorly populated. The thermal dependence of the magnetic susceptibility was fitted by the analytical expression of χ_{chain} for an alternating J_O-J_F $S = 1/2$ reported by Hatfield³³ using the coefficient set for dominating dimers ($J_F \leq 0.4 J_O$). The experimental and fitted plots are shown on Fig.4a. The inter-chain spin-exchange interactions were allowed in the molecular field expansion for the susceptibility χ_{chain}^{MF} at the paramagnetic regime (Eq. 1), with $\theta_{\text{inter}} = zS(S+1)/3 J_{\text{inter}}/k_b$, with the number of surrounding spins $z = 8$, as marked in Fig.1b.

$$\chi_{\text{chain}}^{MF} = \frac{\chi_{\text{chain}}(T)}{1 - \theta_{\text{inter}} \left[\frac{\chi_{\text{chain}}(T)}{C} \right]} \quad (\text{equation 1})$$

Finally, the low temperature paramagnetic tail was fitted using a Curie contribution assigned to V^{3+} ($S=1$) impurities with respect to its “non-Kramers” silent EPR consistent with our blank

spectra. Our best fit assuming $g = 2$, and $J_F/J_O = 5\%$ deduced from our ab-initio DFT calculations, yields $J_O/k_b = 306(3)$ K, $J_F/k_b = 15.3$ K and $J_{inter}/k_b = 21.7$ K with $6.0(5)\%$ of V^{3+} impurity. These correspond well to values calculated by DFT+U for U values in between 2 and 3 eV. The heat capacity measurements also confirms the lack of magnetic ordering between 300K and 2K returning a true 1D-magnetic system. However, the strong J_O suggests that most of the magnetic entropy remains engaged until high temperature and only a weak anomaly is expected but not detected, see $C_p/T(T)$ on Figure 4b. Indeed, besides the predominant AFM dimers across the O_2 bridges, the frustration occurring from J_F and J_{NNN} AFM interactions provides explicit arguments for low-temperature intra-chain spin-frustration. In addition, inter-chain FM J_{ac} and AFM J_a create additional frustrated J_a - J_{ac} - J_{ac} triangles and thus hamper any 3D magnetic ordering and the dimerized topology predominates.

Table 2: experimental and calculated J and E_g values by LDA+U for U ranging between 2 and 4 eV.

J and Eg	d(V-V) \AA	U = 2 eV	U=3eV	U=3.5 eV	U=4 eV	Exp.
LDA+U						
J_O/k_b (K) (1x)	2.93	387.1	231.2	177.9	135.5	306(3)
J_F/k_b (K) (1x)	3.32	21.3	14.8	12.7	10.9	15.3
J_{NNN}/k_b (K) (2x)	4.97	3.9	4.4	4.5	4.5	-
J_a/k_b (K) (4x)	5.75-5.84	37.6	21.1	15.4	10.8	21.7(3)
J_{ac}/k_b (K) (4x)	5.26-5.58	-7.68	-5.6	-10.0	-4.5	
E_g (eV)		1.01	1.55	1.78	2.02	1.5-1.7

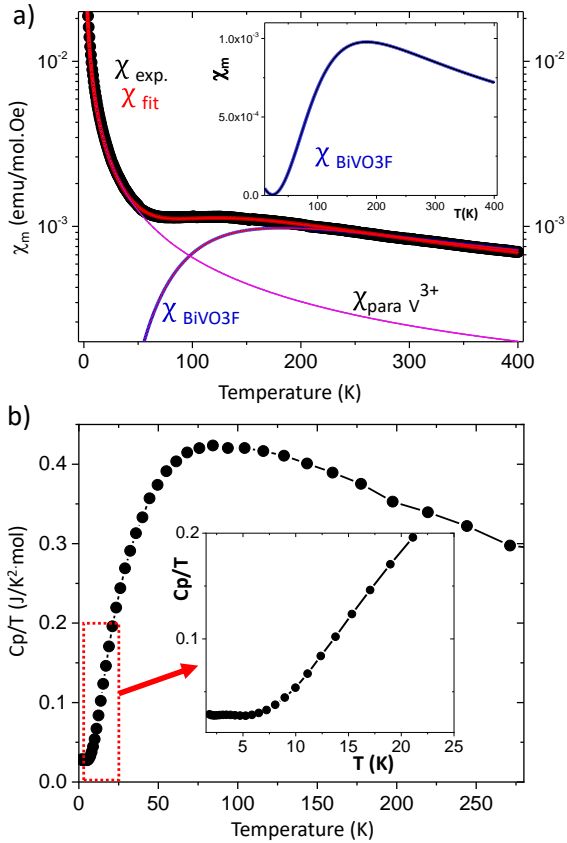


Figure 4: a) Experimental and fitted $\chi(T)$ plot of BiVO_3F . b) $C_p/T(T)$ curve with a zoom in the low temperature domain in the insert proving no magnetic phase transition.

Electronic Band Structure: Besides EHTB calculations, the electronic structure analysis calculated by LDA+U offers a complementary vision in the extended 3D solid, out of discrete molecular orbital levels in the dimer cluster.

The density of states (DOS), and partial density of states (pDOS) are shown on Fig. 5a for $U = 3$ eV in the ferromagnetic state which enables to screen the individual d orbital manifold within a unique type of vanadium in the unit cell. At this U value, it reproduces well the 1.5 - 1.7 eV uv-vis experimental bandgap shown in Fig. 5b. The main Valence Band (VB) between ~ -7 eV and -2 eV displays the same characteristics as what reported for monoclinic BiVO_4 ³⁴. It is primarily of $\text{O}2p$ character, where all O1, O2 and O3 atoms have a distorted triangular plane geometry see figure 2, similar to the oxygen coordinations in BiVO_4 announced of primary importance for its band texture with hybridized sp^2 and unhybridized $2p\pi$ oxygen orbitals. At the top of the VB block, the contribution is mostly from O $2p\pi$ nonbonding states. A sharp contribution of mixed Bi 6s and Bi 6p orbitals at -1.8 eV emphasizes the standard lone pair stereoactivity. The bottom and middle of this VB block contains V 3d states hybridized with F^- and O^{2-} orbitals respectively, as expected for more ionic V-F bonds. Around 1.1 eV above the main VB contribution and just below the Fermi level the $\text{V}^{4+} d^1$ spin up 2B_2 state is trapped in a sharp pocket, similar to monoclinic VO_2 with a spin-Peierls dimerization reminiscent of BiVO_3F .³⁵ The conduction band (CB) is also split, with the very sharp lower part (around 1.5 eV) formed by antibonding vanadium 2E levels mixed with oxygen states and minor contribution of F and Bi p states for both the minority and majority spins. At higher energies (>2.5 eV), the 2B_1 and 2A_1 vanadium states are mixed to Bi and O contributions, according to antibonding V-O and Bi-O σ^* overlap. It results in a band-topology mixing both scheelite- BiVO_4 and monoclinic- VO_2 characteristics, and allows for two allowed sets of $d \rightarrow d$ transitions, experimentally observed and labelled as (1) and (2) in the Figure 5. The concerned localized states are at the top of VB and bottom of the CB similar defect-levels in doped semi-conductors and may serve as carrier traps during photo-excitation. This offers solutions for $3d$ orbitals too high in the conduction band for d^0 -based semiconductors. BiVO_3F bandgap narrowing and $d-d$ transitions favor water splitting allowing the transition and increasing the capture of the visible light, following the strategy of d^n cations doping in BiVO_4 or TiO_2 .¹⁴⁻¹⁷

Only few works have been focused on the magnetic influence on photo-active properties, and concern mainly i) the magnetic photocatalysts to facilitate the catalysts separation from the reactant liquid-phase³⁶ ii) or more recently the suppressing of photoinduced charge recombination via Lorentz force using an external magnetic field.³⁷

The strong spin polarization arising from the spin AFM exchange within dimers may also offer extra advantages. Indeed, It was recently shown for deficient $\text{Ti}_{1-\delta}\text{O}_2$ that spin-polarized electrons can reduce the recombination of photoinduced electron-hole pairs by spin reversal in the CB due to spin-orbit coupling and hyperfine interactions, as observed in deficient TiO_2 ³⁸ and similar to a phosphorence ingredients. In BiVO_3F , an equivalent scenario is available for the excitation restricted in individual dimers, from the singlet $S=0$ to triplet $S=1$. After photo excitation and spin reversal, the electron-hole recombination is thus inhibited by the lack of spin-down in a spin-polarized environment. Figure 5a shows the DOS for vanadium d -levels calculated for an AFM $-up-down-$ spin polarized sequence along the edge-sharing chain very close to the DOS for AFM monoclinic- VO_2 .³⁹ The probability to excite two d^1 electrons in the

same dimer is weak. After reversal of a single excited electron (\downarrow), it must propagate and annihilate with the next excited dimer with down spin-holes (\downarrow) which guaranty carrier diffusion. Of course this is again a “*double-edge sword*”, in that sense that the primary electronic excitation itself is hampered by the strong AFM magnetic exchanges holding robust S=0 dimeric singlets as the stable state.

As detailed by Butler and Ginley⁴⁰, empirical calculations based on Mulliken electronegativities permit to calculate flat band potentials in excellent agreement with measured ones and helps for a preselection of pertinent electrode materials. The CB and VB positions for BiVO₃F were calculated by $E_{VB/CB} = \chi - E^e \pm E_g/2$, χ being the geometric mean value of Mulliken electronegativity of the different atoms, E^e the free electron energy ($E^e = 4.5$ V vs SHE), and E_g the measured band gap of the photocatalyst (~ 1.8 eV) $E_{VB} = 2.75$ V and $E_{CB} = 0.98$ V vs SHE. It is reported in Figure 5c and compared to those calculated for BiVO₄. It shows potentialities for oxygen evolution as an anodic photocatalysts, similar to BiVO₄ as VB lies lower than the O₂/H₂O redox potential. In the actual scope, only the potentiality for photocurrent generation was investigated.

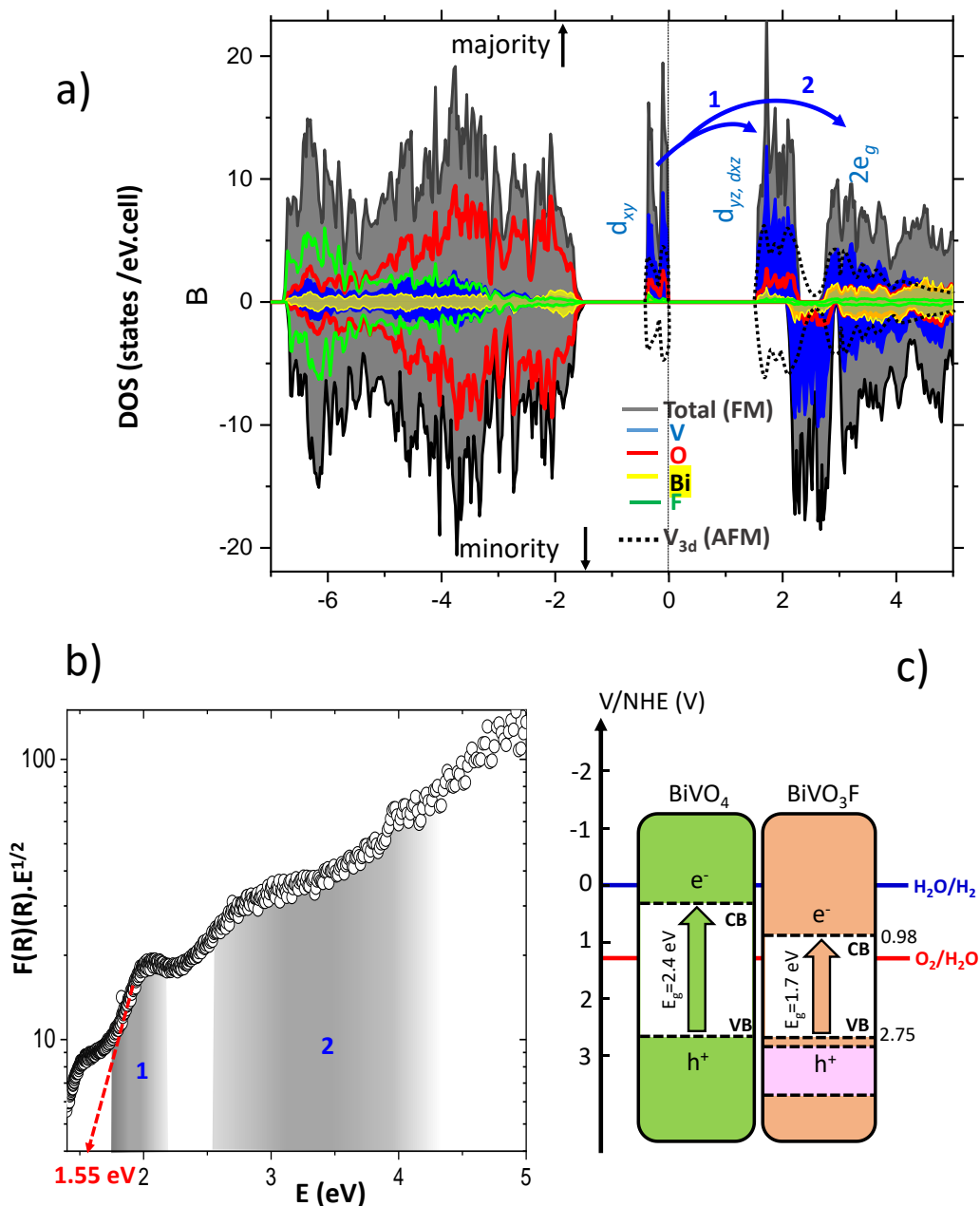


Figure 5. a) Total and atomic resolved projected DOS for BiVO_3F ($U=3$ eV, FM/AFM spin polarized configuration). b) Diffuse-reflectance spectra with a Tauc plot calculation giving $E_g=1.55$ eV the grey areas denote the analogy with the DOS structure. c) Band edge estimation (versus NHE) for BiVO_4 and BiVO_3F .

Photoactivated transport: BiVO_3F shows a positive slope in the Mott-Schottky plot $1/C^2(E)$, as expected for a n-type semiconductor, resulting in a flat band potential $E_{fb} = 0.095$ V vs. Ag/AgCl or 0.684 vs. RHE (pH = 6.5) at $1/C^2=0$ ⁴¹. This potential allows to locate the valence and conduction band edges by knowing E_g and assuming that E_{fb} is lower by 0.1 V of the conduction for n-type semiconductors^{42, 43}. Therefore, the conduction band potential of BiVO_3F

is consistent with the empirical calculated value given previously. Interestingly, in a basic PEC for water splitting, the photoinduced minority carriers are driven to the semiconductor/electrolyte interface, whereas the majority carriers are transported to the counter electrode through the external circuit.⁴⁴ In the case of n-type semiconductor, electrons as the majority carriers are transferred to the counter while holes (the minority carriers) oxidize water to O₂ at the semiconductor surface. Therefore, n-type BiVO₃F possess both the carrier type and VB position for oxygen-evolution, similarly to n-type BiVO₄.

The photoelectrochemical performances of this photoanode were studied in a three-electrode cell (Ag/AgCl as the reference electrode and Pt as the counter electrode) and in 0.1 M Na₂SO₄ solution was used as electrolyte. The chronoamperometry results performed on BiVO₃F thick film are shown in Figure 6b and prove the generation of a modest photocurrent ($< 10^{-1} \mu\text{A}/\text{cm}^2$). The variation of the photocurrent density (Δj) shows better efficiency increasing the irradiation energy, i.e. towards low wavelengths. A significant jump of the response is observed below 590 nm (above $\sim E_g$) which corresponds to the allowed ${}^2B_2 \rightarrow {}^2E$ transitions previously labelled as (1). At this stage, the strong magnetic exchange and poor Bi 6p participation plays in favor of easy electron-hole recombination. On the opposite, the current density, increases drastically below 470 nm (2.6 eV) which corresponds to the allowed ${}^2B_2 \rightarrow {}^2B_1, {}^2A_1$ transitions (2) in the broad upper CB top part, for which the hybridization with Bi states would improve the electron-hole spatial separation and carrier extraction processes. The photocurrent response models rather well the specific CB topology, giving forbidden transitions between 2.2 and 2.5 eV, see Fig. 5a.

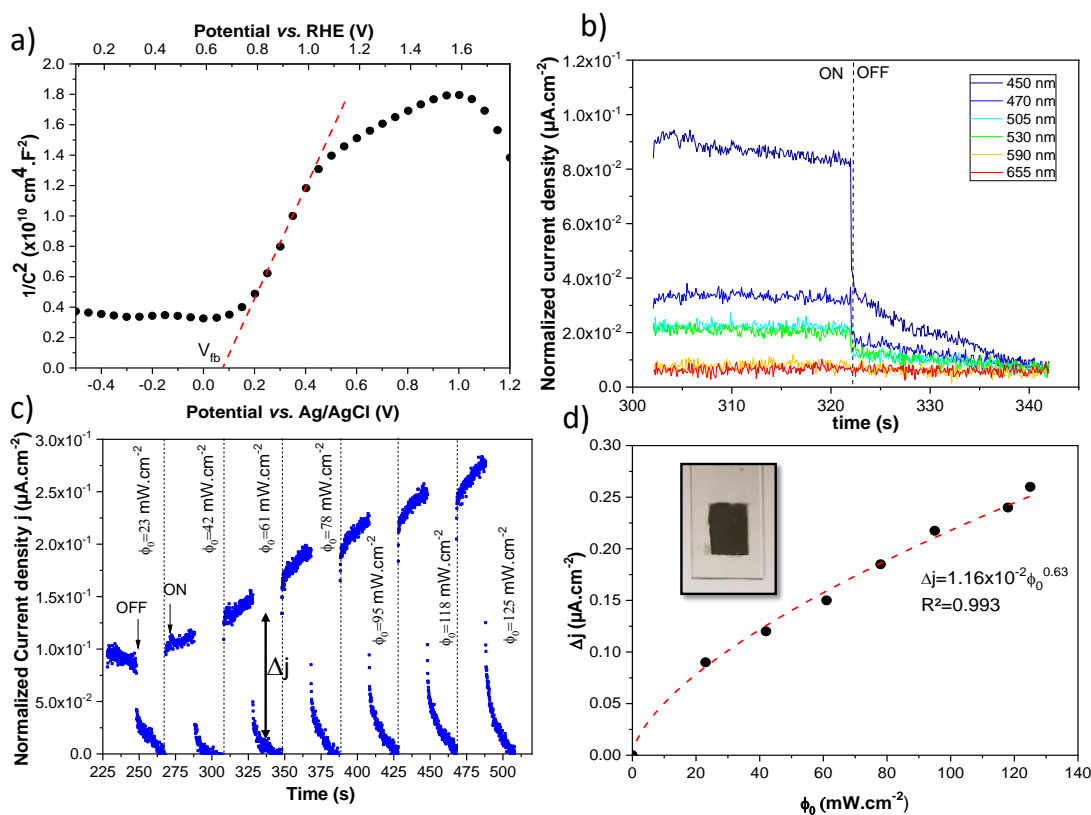


Figure 6. a) Mott-Schottky plot for BiVO₃F film deposited on ITO/Glass collected at 100 Hz (a 0.1 M sodium sulfate solution was used as the electrolyte); b) Chronoamperometry (j - t) in dark and under illumination for different wavelengths with a constant light beam intensity of 23

$mW.cm^{-2}$; c) Variation of normalized current density under illumination or dark depending on the intensity of the luminous flux (450 nm) and with an applied potential of 0.8 V vs. Ag/AgCl; d) Δj vs. ϕ_0 plot and model in dotted lines (inset photograph of the film deposited by drop casting method).

The on/off variation at 450 nm is maximal for a photocurrent density of $0.09 \mu A.cm^{-2}$ with a bias potential of 0.8 V vs. Ag / AgCl and under light intensity (ϕ_0) of $23 mW.cm^{-2}$ (this drops to $0.02 \mu A.cm^{-2}$ for 530 nm with the same luminous power and becomes equal to zero for higher wavelengths). The evolution of the photocurrent Δj with the intensity of luminous flux ($\lambda=450$ nm; $V=0.8$ V vs. Ag/AgCl) is shown in Figure 6c. It was fitted by a power law ($\Delta j=1.6 \times 10^{-2} \phi_0^{0.63}$). The generation rate of photoelectrons by incident light (G_{pe}) is given by the expression^{45,46}:

$$G_{pe} = B_c n_{pe} (n_{pe} + M) \propto \phi_0 \quad (\text{equation 2})$$

Where B_c is the recombination coefficient, n_{pe} is the density of photoelectrons and M is number of impurity levels per cm^3 . For $BiVO_3F$ $n_{pe} \gg M$ and equation (2) follows a power law:

$$\Delta j \propto n_{pe} = \sqrt{G_{pe}/B_c} \propto \phi_0^{1/2} \quad (\text{equation 3})$$

This suggests the dominant photocarrier decay mechanism is from e-h recombination rather than a trap-dominated recombination process. Although the sharp localized CB and VB as traps, spin-polarized dimers and a narrowed band gap will favor longer carrier lifetimes, the dimerized crystal structure and the strong AFM exchanges make a significant photoactivity difficult in our single valent V^{4+} semiconductor, but informs as potentialities and novel concepts for $BiVO_3F$ -type defects in a $BiVO_4$ structure. The similitude of the paired spins in $BiVO_3F$ with the monoclinic VO_2 behavior, is also reminiscent of some exotic features probably detrimental to any efficient charge-hole separation. In photo-excited monoclinic VO_2 a fast collapsing of the bandgap into a metal was observed by time-resolved photoelectron spectroscopy, at the femto-second scale.¹³ This ultra-fast band structure reconstruction corresponds to the typical time announced for electron-holes formation and trapping in semiconducting TiO_2 , suggesting a similar phenomenon in $BiVO_3F$ in spite of its larger bandgap, a major drawback for the further trapping of exciton, if available.

Note that for higher light intensities, the saturation can be achieved. Moreover, the photocurrent transient response follows an exponential type evolution whose time constant increases with the light intensity. Finally, the response under solar excitation of AM1.5G one-sun was also measured showing the appearance of a photocurrent (Figure S6), scaled by the applied bias potential. A change from a crenel- to an exponential-type occurs upon increasing the applied potential.

Concluding remarks: The discovery of novel stoichiometric mixed $X=(O,F)$ compounds in the intensively studied Bi-V-X is quite unexpected enlarging the prism of the various specificities of the parent oxides, e.g. unequalled anionic conductivity in $Bi_2VO_{5.5}$ BIMEVOX Aurivillius derivatives⁴⁷, Bi^{3+} square-planar coordination and field dependent metal-insulator transition in $Bi_xV_8O_{16}$ hollandites^{48, 49}, $BiVO_3F$ is an original vanadyl ($V=O$)²⁺ containing Bi-oxofluoride with alternating F_2 and O_2 μ_2 bridges along magnetically isolated chains. Despite short $V=O$ bonds externally to the chain axis, the crystal structure displays V^{4+} - V^{4+} dimers ($d = 2.93 \text{ \AA}$) leading to $S = 0$ singlet dimers, $J/K_b \sim 300K$, absent of long-range ordering. The

compositional analogy with BiVO_4 and electronic structure arguments question about the photoactivity of BiVO_3F . Despite its modest photoelectronic properties, BiVO_3F provides clues for optimizing the photoanodic response by chemical design: i) according to the chemical composition, filled Bi 6s orbitals hybridized with O 2p raise the VB edge and reduce the bandgap energy in BiVO_4 to $E_g = 2.4 \text{ eV}$ ⁵⁰, this is exaggerated in BiVO_3F ($E_g = 1.7 \text{ eV}$) by the incorporation of $d^1 \text{ V}^{4+}$ species. ii) Theoretically, the visible light capture and conversion to photocurrent could reach $\sim 30\%$ at this bandgap¹⁸. iii) sharp localized d states at the top of the CB and bottom of the VB show analogies with defect carrier traps in d^n doped semiconductors. Additionally, several structural (Bi and V strongly asymmetric coordination, sp^2 oxygen atoms) and electronic band arguments are retained and validate the measured photoelectrical activity. However, the crystal structure itself with strongly coupled magnetic $\text{V}^{4+}\text{-V}^{4+}$ dimers are detrimental for d-d transitions and long electron-hole spatial separation. Further investigation of the electronic characteristic of BiVO_3F are necessary at least in order to draw the $\text{BiVO}_3\text{F}/\text{BiVO}_4$ analogies and contrasts for a clear understanding of photo-carrier specificities. It was observed that as soon as the energy reaches the upper CB zone with Bi hybridization, the photoconversion is greatly improved, which suggest that synthetic routes to antagonist 3-D V^{4+} doped by halogen incorporation opens a promising route for specific components of high-performance photo electric cells. Moreover, contrarily to most of the actual photocatalysts, BiVO_3F film shows no sign of chemical- nor photo-degradation and thus offers clues to design more durable PEC technology. we recall that, we did not observe any sign of chemical degradation nor photodegradation after our photocurrent study.

Experimental

Hydrothermal synthesis: Single crystals were prepared through the hydrothermal route. A mixture of VF_3 (1mmol) and Bi_2O_3 (1 mmol) were added together with 2.5 ml of deionized water and 0.5 ml of HF solution (7.65%) in a 23 ml Teflon lined steel autoclave. Mixture was heated at $230 \text{ }^\circ\text{C}$ for 72 h and then cooled to room temperature. Products were successively washed with deionized water and ethanol and left to dry in air at room temperature. Black crystals were isolated for characterizations.

XRD: Powder XRD was carried out on a Bruker D8 Advanced diffractometer working in Bragg-Brentano geometry and using Cu radiation. The single crystal data collected on a Bruker X8 diffractometer (Ag $K\alpha$ radiation) have treated using the Jana 2006 suite.⁵¹ The powder data have been analyzed using the FULLPROF suite.⁵²

Magnetic measurement: Magnetic data and heat capacities were measured on a Physical Property Measurement System Quantum Design PPMS DynaCool system, using BiVO_3F ground powder.

UV visible spectroscopy: It was measured on a Perkin Elmer Lambda 650 Spectrometer. The bandgap was calculated from the calculation of the Kubelka-Munk $F(R)=(1-R^2)/2R$ function and using Tauc plot ($F(R) * R * E^{1/2}$) versus E, assuming direct allowed transitions.

DFT and EHTB calculations: We performed density functional theory (DFT) band structure calculations using the full-potential local-orbital scheme (FPLO9.00-33).⁵³ applying the local density approximation (LDA + U, U = 2 to 4 eV) with the exchange-correlation potential by Perdew and Wang.⁵⁴ using the Vienna *ab initio* simulation package (VASP)⁵⁵ with the basis set of projected augmented waves⁵⁶. For the calculations of the magnetic exchanges identified in the plain text, we mapped the total energies for a number of collinear spin configurations onto a classical Heisenberg model to yield individual exchange couplings for various U and the effective on-site exchange interaction $J_{\text{eff}} = 1 \text{ eV}$. For the accurate DOS topology, the typical k mesh was $15 \times 15 \times 15$ reduced to 1688 k-points in the the symmetry-irreducible part of the first

Brillouin zone for the crystallographic unit cell using the spin polarized ferromagnetic configuration. The EHTB calculations have been performed using Samoa.⁵⁷

Electrochemistry: Photoelectrochemical properties of BiVO₃F were measured using PGSTAT204 potentiostat/galvanostat (Metrohm) equipped with Electrochemical Impedance Spectroscopy (EIS) Module and coupled with optical bench consisting of low spectral dispersions LEDs or a 150 W Xe lamp (Quantum Design) with AM1.5G filter (to simulate the terrestrial solar spectrum). For LEDs illumination sources, the intensity of the light beam as well as the excitation wavelength could be controlled by NOVA 2.0 software. The photoelectrochemical performance measurements were performed in standard three-electrode cell (Magnetic Mount Photo-electrochemical Cell (Redox.me®) is used in order to obtain a standardized illumination of 1 cm² on the back face of the working electrode) and the electrolyte employed is an aqueous 0.1M Na₂SO₄ solution. The working electrode consists of a thick BiVO₃F film is deposited on ITO/glass Substrate (delta technologies, LTD) by the drop casting method. So, the crushed BiVO₃F powder is added to a mixture of water and *N,N*-Dimethylformamide (DMF) solvents with a 1:1 ratio. The liquid containing the suspension is drop casted on the surface of electrode and a uniform layer is obtained after the solvent evaporation. A Ag/AgCl electrode and Pt wire were used as a reference and a counter electrode, respectively. The measured potentials versus Ag/AgCl electrode were converted to the Reversible Hydrogen Electrode (RHE) scale.

ASSOCIATED CONTENT

Supporting Information. The supporting information is available free of charge on the Website at DOI:

More detailed crystallographic information (with powder refinement data, atomic positions and anisotropic thermal displacement) can be found in supplementary information, with extra details on the synthesis and photo-electrochemical tests.

NOTES

The authors declare no competing financial interest.

ACKNOWLEDGMENT

This work was carried out under the framework of the LOVE-ME project supported by the ANR (Grant ANR ANR-16-CE08-0023). The Fonds Européen de Développement Régional (FEDER), CNRS, Région Hauts-de-France and Ministère de l'Education Nationale, de l'Enseignement Supérieur et de la Recherche are acknowledged for funding the XRD and PPMS equipments. Chevreul Institute (FR 2638), Ministère de l'Education Nationale, de l'Enseignement Supérieur et de la Recherche, Région Hauts-de-France, FEDER are acknowledged for supporting this work. The DIM 1 "Energetic efficiency" of the UArtois is thanked for its financial support for photoelectrochemical measurements. We thank Laurence Burylo, Nora Djelal & Claire Minaud at the UCCS for their technical help. Hiroshi Kageyama and the JSPS Core-to-Core Program (A) Advanced Research Networks (JPJSCCA20200004) are acknowledged for motivating this "anion mixed material research" study.

REFERENCES

- ¹ Deng, D. Transition Metal Oxyfluorides for Next-Generation Rechargeable Batteries. *ChemNanoMat* **2017**, 3 (3), 146–159. <https://doi.org/10.1002/cnma.201600342>.
- ² Inaguma, Y.; Greneche, J. M.; Crosnier-Lopez, M. P.; Katsumata, T.; Calage, Y.; Fourquet, J. L. Structure and Mössbauer Studies of F-O Ordering in Antiferromagnetic Perovskite PbFeO₂F. *Chem. Mater.* **2005**, 17 (6), 1386–1390. <https://doi.org/10.1021/cm048125g>.
- ³ Simon, A.; Ravez, J. The Oxyfluoride Ferroelectrics. *Ferroelectrics* **1980**, 24 (1), 305–307. <https://doi.org/10.1080/00150198008238660>.
- ⁴ Katsumata, T.; Nakashima, M.; Umemoto, H.; Inaguma, Y. Synthesis of the Novel Perovskite-Type Oxyfluoride PbScO₂F under High Pressure and High Temperature. *J. Solid State Chem.* **2008**, 181 (10), 2737–2740. <https://doi.org/10.1016/j.jssc.2008.06.048>.
- ⁵ Lemoine, K.; Lhoste, J.; Hémon-Ribaud, A.; Heidary, N.; Maisonneuve, V.; Guiet, A.; Kornienko, N. Investigation of Mixed-Metal (Oxy)Fluorides as a New Class of Water Oxidation Electrocatalysts. *Chem. Sci.* **2019**, 10 (40), 9209–9218. <https://doi.org/10.1039/c9sc04027g>.
- ⁶ Mitoudi Vagourdi, E.; Müllner, S.; Lemmens, P.; Kremer, R. K.; Johnsson, M. Synthesis and Characterization of the Aurivillius Phase CoBi₂O₂F₄. *Inorg. Chem.* **2018**, 57 (15), 9115–9121. <https://doi.org/10.1021/acs.inorgchem.8b01118>.
- ⁷ Katsumata, T.; Suzuki, R.; Satoh, N.; Suzuki, S.; Nakashima, M.; Inaguma, Y.; Mori, D.; Aimi, A.; Yoneda, Y. Synthesis of New Perovskite-Type Oxyfluorides, BaInO₂F and Comparison of the Structure among Perovskite-Type Oxyfluorides. *J. Solid State Chem.* **2019**, 279 (July), 120919. <https://doi.org/10.1016/j.jssc.2019.120919>.
- ⁸ Leblanc, M.; Maisonneuve, V.; Tressaud, A. Crystal Chemistry and Selected Physical Properties of Inorganic Fluorides and Oxide-Fluorides. *Chem. Rev.* **2015**, 115 (2), 1191–1254. <https://doi.org/10.1021/cr500173c>.
- ⁹ Tressaud, A.; Dance, J.-M. Relationships between Structure and Low-Dimensional Magnetism in Fluorides. In *Structures versus Special Properties*; 2007; pp 87–146. <https://doi.org/10.1007/bfb0111297>.
- ¹⁰ Anke, B.; Rohloff, M.; Willinger, M. G.; Hetaba, W.; Fischer, A.; Lerch, M. Improved Photoelectrochemical Performance of Bismuth Vanadate by Partial O/F-Substitution. *Solid State Sci.* **2017**, 63, 1–8. <https://doi.org/10.1016/j.solidstatesciences.2016.11.004>.
- ¹¹ Akopjan, A. V.; Serov, T. V.; Dolgikh, V. A.; Ardaschnikova, E. I.; Lightfoot, P. A New Anion Conductive Bismuth-Vanadium Oxyfluoride. *J. Mater. Chem.* **2002**, 12 (5), 1490–1494. <https://doi.org/10.1039/b201049f>.
- ¹² Wang, Z.; Huang, X.; Wang, X. Recent Progresses in the Design of BiVO₄-Based Photocatalysts for Efficient Solar Water Splitting. *Catal. Today* **2019**, 335, 31–38. <https://doi.org/10.1016/j.cattod.2019.01.067>.

-
- 13 Wegkamp, D.; Herzog, M.; Xian, L.; Gatti, M.; Cudazzo, P.; McGahan, C. L.; Marvel, R. E.; Haglund, R. F.; Rubio, A.; Wolf, M.; Stähler, J. Instantaneous Band Gap Collapse in Photoexcited Monoclinic VO₂ Due to Photocurrent Doping. *Phys. Rev. Lett.* **2014**, *113* (21). <https://doi.org/10.1103/PhysRevLett.113.216401>.
- 14 Zhao, Z.; Luo, W.; Li, Z.; Zou, Z. Density Functional Theory Study of Doping Effects in Monoclinic Clinobisvanite BiVO₄. *Phys. Lett. Sect. A Gen. At. Solid State Phys.* **2010**, *374* (48), 4919–4927. <https://doi.org/10.1016/j.physleta.2010.10.014>.
- 15 Khan, H.; Swati, I. K. Fe³⁺-Doped Anatase TiO₂ with d-d Transition, Oxygen Vacancies and Ti³⁺ Centers: Synthesis, Characterization, UV-Vis Photocatalytic and Mechanistic Studies. *Ind. Eng. Chem. Res.* **2016**, *55* (23), 6619–6633. <https://doi.org/10.1021/acs.iecr.6b01104>.
- 16 Zhang, Y.; Guo, Y.; Duan, H.; Li, H.; Sun, C.; Liu, H. Facile Synthesis of V⁴⁺ Self-Doped, [010] Oriented BiVO₄ Nanorods with Highly Efficient Visible Light-Induced Photocatalytic Activity. *Phys. Chem. Chem. Phys.* **2014**, *16* (44), 24519–24526. <https://doi.org/10.1039/c4cp03795b>.
- 17 Jiang, H.; Dai, H.; Deng, J.; Liu, Y.; Zhang, L.; Ji, K. Porous F-Doped BiVO₄: Synthesis and Enhanced Photocatalytic Performance for the Degradation of Phenol under Visible-Light Illumination. *Solid State Sci.* **2013**, *17*, 21–27. <https://doi.org/10.1016/j.solidstatesciences.2012.12.009>.
- 18 Jian, J.; Jiang, G.; van de Krol, R.; Wei, B.; Wang, H. Recent Advances in Rational Engineering of Multinary Semiconductors for Photoelectrochemical Hydrogen Generation. *Nano Energy*. 2018, pp 457–480. <https://doi.org/10.1016/j.nanoen.2018.06.074>.
- 19 Ellis, B. L.; Michael Makahnouk, W. R.; Rowan-Weetaluktuk, W. N.; Ryan, D. H.; Nazar, L. F. Crystal Structure and Electrochemical Properties of A₂MPO₄F Fluorophosphates (A = Na, Li; M = Fe, Mn, Co, Ni). *Chem. Mater.* **2010**, *22* (3), 1059–1070. <https://doi.org/10.1021/cm902023h>.
- 20 Hu, S.; Johnsson, M.; Law, J. M.; Bettis, J. L.; Whangbo, M. H.; Kremer, R. K. Crystal Structure and Magnetic Properties of FeSeO₃F - Alternating Antiferromagnetic S = 5/2 Chains. *Inorg. Chem.* **2014**, *53* (8), 4250–4256. <https://doi.org/10.1021/ic5003995>.
- 21 Hu, S.; Johnsson, M. Synthesis and Crystal Structure of Two Synthetic Oxofluoride Framework Compounds - Co₂TeO₃F₂ and Co₂SeO₃F₂. *Dalt. Trans.* **2012**, *41* (41), 12786–12789. <https://doi.org/10.1039/c2dt31188g>.
- 22 Mitoudi-Vagourdi, E.; Papawassiliou, W.; Müllner, S.; Jaworski, A.; Pell, A. J.; Lemmens, P.; Kremer, R. K.; Johnsson, M. Synthesis and Physical Properties of the Oxofluoride Cu₂(SeO₃)F₂. *Inorg. Chem.* **2018**, *57* (8), 4640–4648. <https://doi.org/10.1021/acs.inorgchem.8b00372>.
- 23 Streltsov, S. V.; Khomskii, D. I. Electronic Structure and Magnetic Properties of Pyroxenes (Li,Na) TM (Si,Ge)₂O₆: Low-Dimensional Magnets with 90° Bonds. *Phys. Rev. B - Condens. Matter Mater. Phys.* **2008**, *77* (6). <https://doi.org/10.1103/PhysRevB.77.064405>.
- 24 Gnezdilov, V.; Lemmens, P.; Zvyagin, A. A.; Cheranovskii, V. O.; Lamonova, K.; Pashkevich, Y. G.; Kremer, R. K.; Berger, H. Magnetic Crossover and Complex Excitation Spectrum of the Ferromagnetic/Antiferromagnetic Spin-1/2 Chain System α-TeVO₄. *Phys. Rev. B - Condens. Matter Mater. Phys.* **2008**, *78* (18). <https://doi.org/10.1103/PhysRevB.78.184407>.

- 25 Koo, H. J.; Whangbo, M. H. Spin Dimer Analysis of the Magnetic Structures of $A_2V_3O_9$ ($A = Ba, Sr$) and η - $Na_9V_{14}O_{35}$: Importance of the $V^{4+}-O\cdots O-V^{4+}$ Super-Superexchange Interactions Mediated by the $O-V^{5+}-O$ Bridges. *Solid State Sci.* **2007**, *9* (9), 824–832. <https://doi.org/10.1016/j.solidstatesciences.2007.06.013>.
- 26 Aldous, D. W.; Lightfoot, P. Crystallisation of Some Mixed Na/V and K/V Fluorides by Solvothermal Methods. *Solid State Sci.* **2009**, *11* (2), 315–319. <https://doi.org/10.1016/j.solidstatesciences.2008.09.003>.
- 27 Pedersen, K. S.; Sigrist, M.; Weihe, H.; Bond, A. D.; Thuesen, C. A.; Simonsen, K. P.; Birk, T.; Mutka, H.; Barra, A. L.; Bendix, J. Magnetic Interactions through Fluoride: Magnetic and Spectroscopic Characterization of Discrete, Linearly Bridged $[Mn^{III}_2(\mu-F)F_4(Me_3tacn)_2](PF_6)$. *Inorg. Chem.* **2014**, *53* (10), 5013–5019. <https://doi.org/10.1021/ic500049w>.
- 28 Goodenough, J. B.; Dutta, G.; Manthiram, A. Lattice Instabilities near the Critical V-V Separation for Localized versus Itinerant Electrons in LiV_1-XY_2 ($M=Cr$ or Ti) Li_1-XVO_2 . *Phys. Rev. B* **1991**, *43* (13), 10170–10178. <https://doi.org/10.1103/PhysRevB.43.10170>.
- 29 Lakshmi, S.; Endo, T.; Siva, G. Electronic (Absorption) Spectra of 3d Transition Metal Complexes. In *Advanced Aspects of Spectroscopy*; 2012. <https://doi.org/10.5772/48089>.
- 30 Wang, C.; Wadhwa, A.; Cui, S.; Ma, R.; Qiao, X.; Fan, X.; Zhang, X. Dual Mode Temperature Sensing through Luminescence Lifetimes of F- and O-Coordinated Cr^{3+} Sites in Fluorosilicate Glass-Ceramics. *RSC Adv.* **2017**, *7* (83), 52435–52441. <https://doi.org/10.1039/c7ra10864h>.
- 31 Kashimoto, Y.; Yonezawa, K.; Meissner, M.; Gruenewald, M.; Ueba, T.; Kera, S.; Forker, R.; Fritz, T.; Yoshida, H. The Evolution of Intermolecular Energy Bands of Occupied and Unoccupied Molecular States in Organic Thin Films. *J. Phys. Chem. C* **2018**, *122* (22), 12090–12097. <https://doi.org/10.1021/acs.jpcc.8b02581>.
- 32 Tsirlin, A. A.; Janson, O.; Rosner, H. Unusual Ferromagnetic Superexchange in $CdVO_3$: The Role of Cd. *Phys. Rev. B - Condens. Matter Mater. Phys.* **2011**, *84* (14). <https://doi.org/10.1103/PhysRevB.84.144429>.
- 33 Hall, J. W.; Marsh, W. E.; Weller, R. R.; Hatfield, W. E. Exchange Coupling in the Alternating-Chain Compounds Catena - Di- μ - Chloro-Bis (4-Methylpyridine) Copper (II), Catena - Di- μ - Bromo-Bis (N-Methylimidazole) Copper (II), Catena -[Hexanedione Bis(Thiosemicarbazone)]Copper(II), and Catena -[Octanedione]. *Inorg. Chem.* **1981**, *20* (4), 1033–1037. <https://doi.org/10.1021/ic50218a017>.
- 34 Cooper, J. K.; Gul, S.; Toma, F. M.; Chen, L.; Glans, P. A.; Guo, J.; Ager, J. W.; Yano, J.; Sharp, I. D. Electronic Structure of Monoclinic $BiVO_4$. *Chem. Mater.* **2014**, *26* (18), 5365–5373. <https://doi.org/10.1021/cm5025074>.
- 35 Shao, Z.; Cao, X.; Luo, H.; Jin, P. Recent Progress in the Phase-Transition Mechanism and Modulation of Vanadium Dioxide Materials. *NPG Asia Materials*. July 25, 2018, pp 581–605. <https://doi.org/10.1038/s41427-018-0061-2>.
- 36 Jacinto, M. J.; Ferreira, L. F.; Silva, V. C. Magnetic Materials for Photocatalytic Applications—a Review. *Journal of Sol-Gel Science and Technology*. 2020. <https://doi.org/10.1007/s10971-020-05333-9>.

-
- 37 Gao, W.; Lu, J.; Zhang, S.; Zhang, X.; Wang, Z.; Qin, W.; Wang, J.; Zhou, W.; Liu, H.; Sang, Y. Suppressing Photoinduced Charge Recombination via the Lorentz Force in a Photocatalytic System. *Adv. Sci.* **2019**, *6* (18). <https://doi.org/10.1002/advs.201901244>.
- 38 Pan, L.; Ai, M.; Huang, C.; Yin, L.; Liu, X.; Zhang, R.; Wang, S.; Jiang, Z.; Zhang, X.; Zou, J. J.; Mi, W. Manipulating Spin Polarization of Titanium Dioxide for Efficient Photocatalysis. *Nat. Commun.* **2020**, *11* (1). <https://doi.org/10.1038/s41467-020-14333-w>.
- 39 Stahl, B.; Bredow, T. Critical Assessment of the DFT + U Approach for the Prediction of Vanadium Dioxide Properties. *J. Comput. Chem.* **2020**, *41* (3), 258–265. <https://doi.org/10.1002/jcc.26096>.
- 40 Butler, M. A.; Ginley, D. S. Prediction of Flatband Potentials at Semiconductor-Electrolyte Interfaces from Atomic Electronegativities. *J. Electrochem. Soc.* **1978**, *125* (2), 228–232. <https://doi.org/10.1149/1.2131419>.
- 41 Bott, A. W. Electrochemistry of Semiconductors. *Curr. Sep.* **1998**, *17* (3), 87–91. https://doi.org/10.2355/tetsutohagane1955.76.9_1423.
- 42 Kalanur, S. S. Structural, Optical, Band Edge and Enhanced Photoelectrochemical Water Splitting Properties of Tin-Doped WO₃. *Catalysts* **2019**, *9* (5). <https://doi.org/10.3390/catal9050456>.
- 43 Matsumoto, Y.; Omae, M.; Watanabe, I.; Sato, E. Photoelectrochemical Properties of the Zn-Ti-Fe Spinel Oxides. *J. Electrochem. Soc.* **1986**, *133* (4), 711–716. <https://doi.org/10.1149/1.2108660>.
- 44 Walter, M. G.; Warren, E. L.; McKone, J. R.; Boettcher, S. W.; Mi, Q.; Santori, E. A.; Lewis, N. S. Solar Water Splitting Cells. *Chem. Rev.* **2010**, *110* (11), 6446–6473. <https://doi.org/10.1021/cr1002326>.
- 45 Moss, T.S. Photoconductivity in the elements. New York, Academic Press, 1952
- 46 Ullrich, B.; Xi, H. Photocurrent Limit in Nanowires. *Opt. Lett.* **2013**, *38* (22), 4698. <https://doi.org/10.1364/ol.38.004698>.
- 47 Lazure, S.; Vernochet, C.; Vannier, R. N.; Nowogrocki, G.; Mairesse, G. Composition Dependence of Oxide Anion Conduction in the BIMEVOX Family. *Solid State Ionics* **1996**, *90* (1–4), 117–123. [https://doi.org/10.1016/s0167-2738\(96\)00412-2](https://doi.org/10.1016/s0167-2738(96)00412-2).
- 48 Abraham, F.; Mentre, O. Bi_{1.7}V₈O₁₆: The First Bi-Hollandite-Type Compound. *J. Solid State Chem.* **1994**, *109* (1), 127–133. <https://doi.org/10.1006/jssc.1994.1082>.
- 49 Larson, A. M.; Wilfong, B.; Moetakef, P.; Brown, C. M.; Zavalij, P.; Rodriguez, E. E. Metal-Insulator Transition Tuned by Magnetic Field in Bi_{1.7}V₈O₁₆ Hollandite. *J. Mater. Chem. C* **2017**, *5* (20), 4967–4976. <https://doi.org/10.1039/c7tc00487g>.
- 50 Walsh, A.; Yan, Y.; Huda, M. N.; Al-Jassim, M. M.; Wei, S. H. Band Edge Electronic Structure of BiVO₄: Elucidating the Role of the Bi s and V d Orbitals. *Chem. Mater.* **2009**, *21* (3), 547–551. <https://doi.org/10.1021/cm802894z>.

- 51 Petříček, V.; Dušek, M.; Palatinus, L. Crystallographic Computing System JANA2006: General Features. *Zeitschrift für Kristallographie*. 2014, pp 345–352. <https://doi.org/10.1515/zkri-2014-1737>.
- 52 Rodríguez-Carvajal, J. Recent Advances in Magnetic Structure Determination by Neutron Powder Diffraction. *Phys. B Phys. Condens. Matter* **1993**, 192 (1–2), 55–69. [https://doi.org/10.1016/0921-4526\(93\)90108-I](https://doi.org/10.1016/0921-4526(93)90108-I).
- 53 Eschrig, H. Full-Potential Nonorthogonal Local-Orbital Minimum-Basis Band-Structure Scheme. *Phys. Rev. B - Condens. Matter Mater. Phys.* **1999**, 59 (3), 1743–1757. <https://doi.org/10.1103/PhysRevB.59.1743>.
- 54 Perdew, J. P.; Wang, Y. Accurate and Simple Analytic Representation of the Electron-Gas Correlation Energy. *Phys. Rev. B* **1992**, 45 (23), 13244–13249. <https://doi.org/10.1103/PhysRevB.45.13244>.
- 55 Kresse, G.; Hafner, J. Ab Initio Molecular Dynamics for Liquid Metals. *Phys. Rev. B* **1993**, 47 (1). <https://doi.org/10.1103/PhysRevB.47.558>.
- 56 Blöchl, P. E. Projector Augmented-Wave Method. *Phys. Rev. B* **1994**, 50 (24), 17953–17979. <https://doi.org/10.1103/PhysRevB.50.17953>.
- 57 D. Dai, J. Ren, W. Liang and H. Whangbo, SAMOA (Structure and Molecular Orbital Analyzer).

For Table of Content Only

